Contents lists available at ScienceDirect

Applied Catalysis B: Environmental

Noble metal-free MoS_2 modified $Mn_{0.25}Cd_{0.75}S$ for highly efficient visible-light driven photocatalytic H_2 evolution

Qun-Zeng Huang [a,b], Yan Xiong [b], Qian Zhang [a], Hong-Chang Yao [a,*], Zhong-Jun Li [a,*]

[a] College of Chemistry and Molecular Engineering, Zhengzhou University, Zhengzhou 450001, PR China
[b] College of Chemistry and Pharmaceutical Engineering, Engineering Technology Research Center of Henan Province for Solar Catalysis, Nanyang Normal University, Nanyang 473061, PR China

ABSTRACT

Development of noble metal-free and highly efficient co-catalyst that endows semiconductor materials with high performance is of great significance towards enhancing photocatalytic H_2 evolution. Herein, a series of novel $Mn_{0.25}Cd_{0.75}S/MoS_2$ composites have been successfully prepared by a facile one-step hydrothermal method. The photocatalytic activity of the as-prepared photocatalysts for H_2 production from water splitting under visible-light irradiation ($\lambda \geq 400\,nm$) was investigated. The results showed that $Mn_{0.25}Cd_{0.75}S/MoS_2$ heterostructured composites have a higher photocatalytic activity than $Mn_{0.25}Cd_{0.75}S$, implying that the intimate interfacial contact between $Mn_{0.25}Cd_{0.75}S$ and MoS_2 facilitates electron transfer from $Mn_{0.25}Cd_{0.75}S$ to MoS_2, thus promoting the separation of photogenerated charge carriers and providing more active sites for H_2 evolution reaction. The introduction of noble metal-free MoS_2 co-catalyst led to a remarkable improvement in the photocatalytic H_2 evolution activity of $Mn_{0.25}Cd_{0.75}S$, and the content of MoS_2 in composite had an important influence on the photocatalytic activity. It was confirmed that 0.7 wt% of MoS_2 loading content achieves a maximum photocatalytic H_2 evolution rate of 12.47 mmol g^{-1} h^{-1}, which was much higher than that of $Mn_{0.25}Cd_{0.75}S$ and also slightly higher than that of $Mn_{0.25}Cd_{0.75}S/Pt$ (1.0 wt%). This work revealed that low cost MoS_2 could replace noble metal Pt as a highly efficient co-catalyst in enhancing the photocatalytic activity of semiconductor materials.

© 2017 Elsevier B.V. All rights reserved.

1. Introduction

Photocatalytic H_2 evolution over semiconductor has been widely regarded as one of the most promising strategies to solve the increasing global energy crisis and environmental problems. Ever since the pioneering discovery of photocatalytic water splitting by Fujishima and Honda in 1972 [1], tremendous semiconductor materials have been explored for H_2 production from water splitting. As one of the most well-known semiconductors, cadmium sulfide (CdS), has attracted tremendous interest in the photocatalytic H_2 evolution due to its sufficient narrow band gap ($\sim$2.4 eV) and high activity under visible light [2–5]. However, its further application toward water splitting is limited by severe photocorrosion and fast recombination of photogenerated charge carriers under visible light [6–8]. An effective way to enhance the photo-

catalytic activity of CdS is to combine with other metal sulfides to make multi-component solid solutions such as $Zn_xCd_{1-x}S$ [9,10], $Mn_xCd_{1-x}S$ [11–13], $(CuIn)_xCd_{2(1-x)}S_2$ [14], $Zn_{1-x}Cd_xIn_2S_4$ [15,16], $Cd_xCu_yZn_{1-x-y}S$ [17], et al. Among them, $Mn_xCd_{1-x}S$ solid solution exhibits higher photocatalytic performance as well as stability than pure CdS because its band gap could be readily tuned by adjusting the value of x to meet the requirement of photocatalytic H_2 evolution. For example, Liu et al. have reported that $Mn_xCd_{1-x}S$ solid solution exhibits a remarkable photocatalytic H_2 evolution activity and good photocatalytic stability by adjusting x value [12]. Although the conduction band position and the band gap of $Mn_{1-x}Cd_xS$ solid solution can be modified to improve the photocatalytic property, the rapid recombination of photoexcited charge carriers still remains a key problem restricting its practical applications. Therefore, the photocatalytic activity of $Mn_xCd_{1-x}S$ still needs to be further improved.

To further upgrade the effectiveness of $Mn_xCd_{1-x}S$ solid solution towards photocatalytic H_2 evolution, several strategies have been employed to reduce its charge recombination, including doping with transition metal of Ni [18], Cu [18] and Ag [19], or constructing

heterojunction with g-C_3N_4 [20]. In addition, co-catalyst modification is also crucial for the enhancement of photocatalytic H_2 evolution activity because it not only could promote the separation of photogenerated charge carriers but also afford the low activation potentials as well as abundant active sites for H_2 evolution [21–27]. Currently, noble metal Pt is widely considered as an effective co-catalyst for promoting photocatalytic H_2 evolution reaction [28–30]. However, the wild use of noble metals is restricted by its high cost. Therefore, it is of significance to develop highly efficient and low-cost noble metal-free co-catalysts for enhancing the photocatalytic activity of $Mn_xCd_{1-x}S$ solid solution. Until now, only Liu and co-workers [31] found that the highest H_2 production rate of 419.3 μmol h^{-1} could be realized by loading 0.3 wt% NiS on the surface of $Mn_{0.5}Cd_{0.5}S$ under visible light irradiation. From the viewpoint of practical application, it is necessary to make great effort to further exploit and develop the $Mn_xCd_{1-x}S$ system based on co-catalyst modification for enhancing its photocatalytic H_2 evolution activity.

Recently, molybdenum disulfide (MoS_2) has attracted much attention as a noble metal-free, low-cost and abundant co-catalyst, which is comparative and even superior to noble metal for enhancing the photocatalytic H_2 evolution activity of photocatalysts. For example, Zong's group [32] confirmed that the H_2 evolution rate of CdS modified with MoS_2 is significantly higher than that of pure CdS, and even higher than that loaded with various noble metal co-catalysts such as Pt, Ru, Rh, Pd and Au. Generally, as a more effective co-catalyst, MoS_2 not only serves as an electron sink to suppress the recombination of electron–hole pairs, but also offers highly accessible reactive sites, dramatically facilitating photocatalytic H_2 evolution reaction [21,22,24–26,33–36]. Previous studies have suggested that the strong interfacial contact between MoS_2 and other semiconductor is essential for the efficient migration and separation of photogenerated charge carriers from semiconductor to MoS_2 [32]. Therefore, it is expected that the modification of $Mn_xCd_{1-x}S$ solid solution with layered MoS_2 would promote the separation of photoexcited electron–hole pairs and offer more active sites for H_2 generation. To the best of our knowledge, there is no report on the application of $Mn_xCd_{1-x}S$ with MoS_2 as a co-catalyst for photocatalytic H_2 evolution.

In this study, a series of $Mn_xCd_{1-x}S$ solid solutions were synthesized via a facile hydrothermal route. The value of x in $Mn_xCd_{1-x}S$ solid solution could be easily adjusted by changing the amount of its sources. The as-prepared pristine $Mn_{0.25}Cd_{0.75}S$ solid solution demonstrated the best photocatalytic performance (as discussed later). Thus, $Mn_{0.25}Cd_{0.75}S$ solid solution was used in the following study. Herein, for the first time, we reported the synthesis of a series of $Mn_{0.25}Cd_{0.75}S/MoS_2$ composites with different MoS_2 contents by a facile one-step hydrothermal method with less energy consumption. The obtained $Mn_{0.25}Cd_{0.75}S/MoS_2$ composites exhibited significantly enhanced visible-light driven photocatalytic performance for H_2 evolution as compared with pure $Mn_{0.25}Cd_{0.75}S$. Moreover, the results showed that MoS_2 has a good performance as a co-catalyst that exceeds that of Pt metal towards photocatalytic H_2 evolution under visible light irradiation. Based on the experimental results, a possible mechanism of the enhanced photocatalytic activity over $Mn_{0.25}Cd_{0.75}S/MoS_2$ was also proposed.

2. Experimental section

2.1. Materials

Manganese acetate tetrahydrate ($Mn(CH_3COO)_2 \cdot 4H_2O$), cadmium acetate dihydrate ($Cd(CH_3COO)_2 \cdot 2H_2O$), sodium molybdate (VI) dehydrate ($Na_2MoO_4 \cdot 2H_2O$), thioacetamide (TAA), sodium sulfide nonahydrate ($Na_2S \cdot 9H_2O$) and sodium sulfite (Na_2SO_3) and

chloroplatinic acid ($H_2PtCl_6 \cdot 6H_2O$, 37.5% Pt basis) were obtained from Aladdin Reagent Co., Ltd. All reagents used are of analytical grade and were used without further purification.

2.2. Synthesis of $Mn_{0.25}Cd_{0.75}S/MoS_2$ composites

The $Mn_{0.25}Cd_{0.75}S/MoS_2$ composites with different loading content of MoS_2 were prepared by using a simple newly-developed one-pot hydrothermal synthesis method. In a typical procedure, 2.25 mmol of $Mn(CH_3COO)_2 \cdot 4H_2O$, 6.75 mmol of $Cd(CH_3COO)_2 \cdot 2H_2O$ and excessive amounts of TAA were dissolved into 40 mL deionized water with constant stirring. Then a varying amount of $Na_2MoO_4 \cdot 2H_2O$ were added. After further stirring for 30 min, the mixture was transferred into a 100 mL Teflon-lined stainless steel autoclave and maintained at 200 °C for 24 h under autogenous pressure. After cooling, the precipitates were collected by centrifugation, washed with deionized water and ethanol for several times. The final product was obtained after drying in a vacuum oven at 60 °C. For comparison, $Mn_{0.25}Cd_{0.75}S$ and other $Mn_xCd_{1-x}S$ ($0 \leq x \leq 1$) samples were synthesized following the same procedure except for no addition of $Na_2MoO_4 \cdot 2H_2O$, and the dosage of $Mn(CH_3COO)_2 \cdot 4H_2O$ and $Cd(CH_3COO)_2 \cdot 2H_2O$ was 9x and 9(1 − x) mmol, respectively. In addition, pure MoS_2 was also prepared using the same hydrothermal method without the addition of $Mn(CH_3COO)_2 \cdot 4H_2O$ and $Cd(CH_3COO)_2 \cdot 2H_2O$.

The actual atomic ratio of Mn^{2+}/Cd^{2+} in the as-prepared $Mn_xCd_{1-x}S$ solid solution and $Mn_{0.25}Cd_{0.75}S/MoS_2$ composite, together with the actual loading content of MoS_2 in $Mn_{0.25}Cd_{0.75}S/MoS_2$ composite were measured by inductively coupled plasma atomic emission spectroscopy (ICP-AES), and the analytical results were given in Table S1 and Table S2. As can be seen, the obtained ICP-AES results were almost consistent with the nominal values. For the sake of convenience, all the samples were addressed with their nominal value.

2.3. Characterization

Elemental measurements of Mn, Cd and Mo were determined by ICP-AES analysis using a Leeman Labs PROFILE SPEC spectrometer. X-ray diffraction (XRD) spectra were acquired with a D8 Advance X-ray diffractometer at room temperature using Cu Kα radiation. Field emission scanning electron microscopy (FE-SEM) images were recorded by a JEOL JSM-7001F field emission scanning electron microscope. Transmission electron microscopy (TEM) and high-resolution transmission electron microscopy (HRTEM) images were recorded by a JEOL JEM-2100F field emission electron microscope. X-ray photoelectron spectroscopy (XPS) data were acquired using a Kratos AXIS HIS 165 spectrometer with a monochromatized Al KR X-ray source (1486.71 eV photons). UV–vis diffusive reflectance spectra (UV–vis DRS) were performed by a Hitachi UH4150 UV–vis/NIR spectrophotometer equipped with an integrating sphere. N_2 adsorption–desorption isotherms and pore-size distributions were obtained on a Micromeritics Tri-Star II 3020 surface area analyzer at 77.35 K. Photoluminescence (PL) spectra and time resolved photoluminescence (TRPL) spectra of the solid samples were recorded on an Edinburgh FLS980 fluorescence spectrofluorometer.

2.4. Photoelectrochemical measurements

Electrochemical measurements were performed on a CHI660E electrochemical instrument with a standard 3-electrode system. The Ag/AgCl (saturated KCl) and Pt foil were used as the reference electrode and counter electrode, respectively. The working electrode was prepared as follows: 10 mg of the as-prepared photocatalyst was suspended in a mixed solution of ethanol (2 mL)

and 0.1 wt% Nafion solution (20 uL) and then dip-coated onto an indium tin oxide (ITO) glass electrode. The coated area on the ITO glass was controlled to be 0.25 cm^2. The film was dried in air and subsequently calcined at 120 °C for 6 h. The photocurrent response was obtained using a 300 W Xe lamp with a UV-cut off filter ($\lambda \geq 400$ nm) as the light source and Na$_2$SO$_4$ (0.5 mol L^{-1}) aqueous solution was used as the electrolyte. Electrochemical impedance spectroscopy (EIS) measurements were determined at an AC voltage magnitude of 5 mV with the frequency range of 10^5 to 0.1 Hz.

2.5. Photocatalytic activity test

Photocatalytic H$_2$ evolution reactions were carried out in an online CEL-SPH2N photocatalysis reaction system (CEAULIGHT, Science and Technology Ltd, Beijing, China) with a 500 mL quartz photoreactor connected to a closed gas circulation and evacuation system, using a 300 W Xe lamp, equipped with an optical 400 nm cut-off filter. In a typical experiment, 50 mg of photocatalyst powder was suspended in a 100 mL of mixed solution containing Na$_2$S (0.5 mol L^{-1}) and Na$_2$SO$_3$ (0.5 mol L^{-1}) as a sacrificial electron donor. The reactant solution was thoroughly degassed under flowing high-purity N$_2$ for 15 min prior to H$_2$ evolution experiment. The evolved H$_2$ was analyzed automatically every 1 h through a gas chromatographer (GC-7920) equipped with a thermal conductivity detector with high-purity N$_2$ as a carrier gas. The recycling test of photocatalytic H$_2$ evolution over the as-prepared photocatalyst was done as follows. Typically, after the reaction of the first run under visible light irradiation, the photocatalyst was separated by filtration and washed with deionized water three times. Then, 100 mL of the fresh 0.5 mol L^{-1} Na$_2$S-Na$_2$SO$_3$ aqueous solution was mixed with this used photocatalyst to subject it to the second run photocatalytic activity test. Analogously, the subsequent five runs of photocatalytic recycling tests were performed. The apparent quantum efficiency (AQE) for H$_2$ evolution was measured under the same photocatalytic reaction conditions except that a 420 nm band-pass filter was used instead of the UV cut-off filter. The number of incident photons was measured using a power meter (Thorlabs PM100D). The AQE was calculated according to the following equation:

$$AQE = \frac{2 \times \text{the number of evolved H}_2 \text{ molecules}}{\text{the number of photons}} \times 100\%$$

3. Results and discussion

3.1. XRD analysis

The phase crystallinity and purity of the as-prepared samples were investigated by XRD analysis, displayed in Fig. 1. Fig. 1a

exhibited XRD patterns of the as-prepared CdS (x = 0), Mn$_x$Cd$_{1-x}$S (0.05 ≤ x ≤ 0.45) solid solutions together with the standard diffraction patterns of CdS and γ-MnS. It was clearly seen that the diffraction peaks of CdS (x = 0) sample are consistent with a hexagonal wurtzite phase of CdS (JCPDS 65-3414). No other crystalline impurities were detected, indicating that the CdS crystallizes in the pure hexagonal wurtzite form. Interestingly, the diffraction peaks of the Mn$_x$Cd$_{1-x}$S products were shifted toward higher diffraction angles from hexagonal CdS to hexagonal γ-MnS (JCPDS 40-1289) with the increase of x value from 0.05 to 0.45. Some of the similar phenomena have also been reported [12,20,35]. The successive shifts in the XRD patterns indicated that the as-prepared samples were not a mixture of CdS and MnS, but were attributable of a Mn$_x$Cd$_{1-x}$S (0.05 ≤ x ≤ 0.45) solid solution. It is considered that the Mn^{2+} incorporated in the CdS lattice or entered its interstitial sites because the radii of Mn^{2+} ion (0.46 Å) is smaller than that of Cd^{2+} (0.97 Å). The lattice constants ($a = b$, c) for the as-prepared CdS and Mn$_x$Cd$_{1-x}$S (0.05 ≤ x ≤ 0.45) solid solutions were determined by the MDI Jade5.0 software. The obtained lattice parameters were listed in Table S3. The lattice parameter a and c for the as-prepared CdS unit cell was 4.1296 Å and 6.7128 Å, respectively, which was consistent with the standard data of 4.132 Å and 6.734 Å (JCPDS 65-3414). Meanwhile, the lattice parameters a and c were found to decrease almost linearly with the increase of Mn mole fraction (Fig. S1). The result was in accord with Vegard's law, indicating a homogeneous solid solution structure of Mn$_x$Cd$_{1-x}$S [37–39]. With further increasing the x value from 0.55 to 0.95 in the Mn$_x$Cd$_{1-x}$S, some diffraction peaks of a-MnS appeared, indicating that the α-MnS impurities exist in the samples (Fig. S2). It is worth noting that the XRD peaks of the pure MnS (x = 1) sample can be indexed to the cubic a-MnS phase with rock salt type (JCPDS 06-0518), which can be connected with hydrothermal temperature of 200 °C because unstable γ-MnS is easily transformed into α phase MnS at high temperature or pressure [40,41].

Fig. 1b showed XRD patterns of the as-prepared MoS$_2$ and Mn$_{0.25}$Cd$_{0.75}$S/MoS$_2$ composites with different loading content of MoS$_2$. The as-prepared MoS$_2$ sample displayed the diffraction peaks at 14.24°, 33.09°, 49.54° and 57.02°, which was responding to the (002), (100), (105) and (110) phase of a hexagonal MoS$_2$ (PDF No. 75-1539), respectively. However, no obvious diffraction peaks of MoS$_2$ could be clearly identified in the Mn$_{0.25}$Cd$_{0.75}$S/MoS$_2$ composites due to the low content of MoS$_2$. Therefore, the results suggested that the deposition of MoS$_2$ did not affect the crystalline structure of Mn$_{0.25}$Cd$_{0.75}$S solid solution.

3.2. SEM and TEM analysis

The size and morphology of as-prepared Mn$_{0.25}$Cd$_{0.75}$S and Mn$_{0.25}$Cd$_{0.75}$S/MoS$_2$-0.7 wt% composite were investigated through
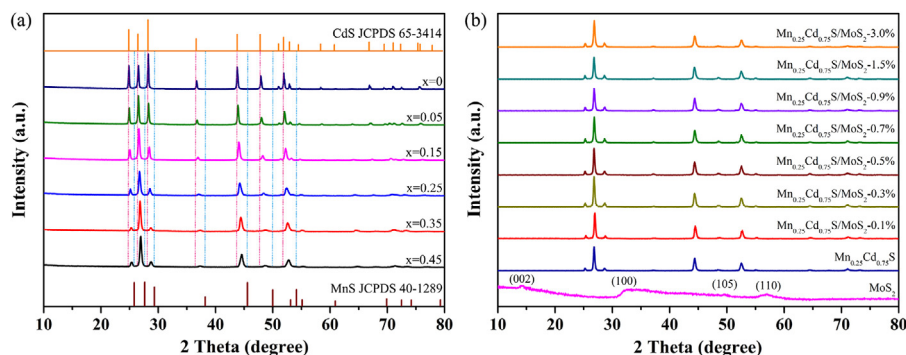

Fig. 1. (a) XRD patterns of the as-prepared CdS (x = 0), Mn$_x$Cd$_{1-x}$S solid solutions (0.05 ≤ x ≤ 0.45) together with the standard diffraction patterns of CdS and γ-MnS, (b) XRD patterns of the as-prepared MoS$_2$ and Mn$_{0.25}$Cd$_{0.75}$S/MoS$_2$ composites loading with different weight ratios of MoS$_2$.
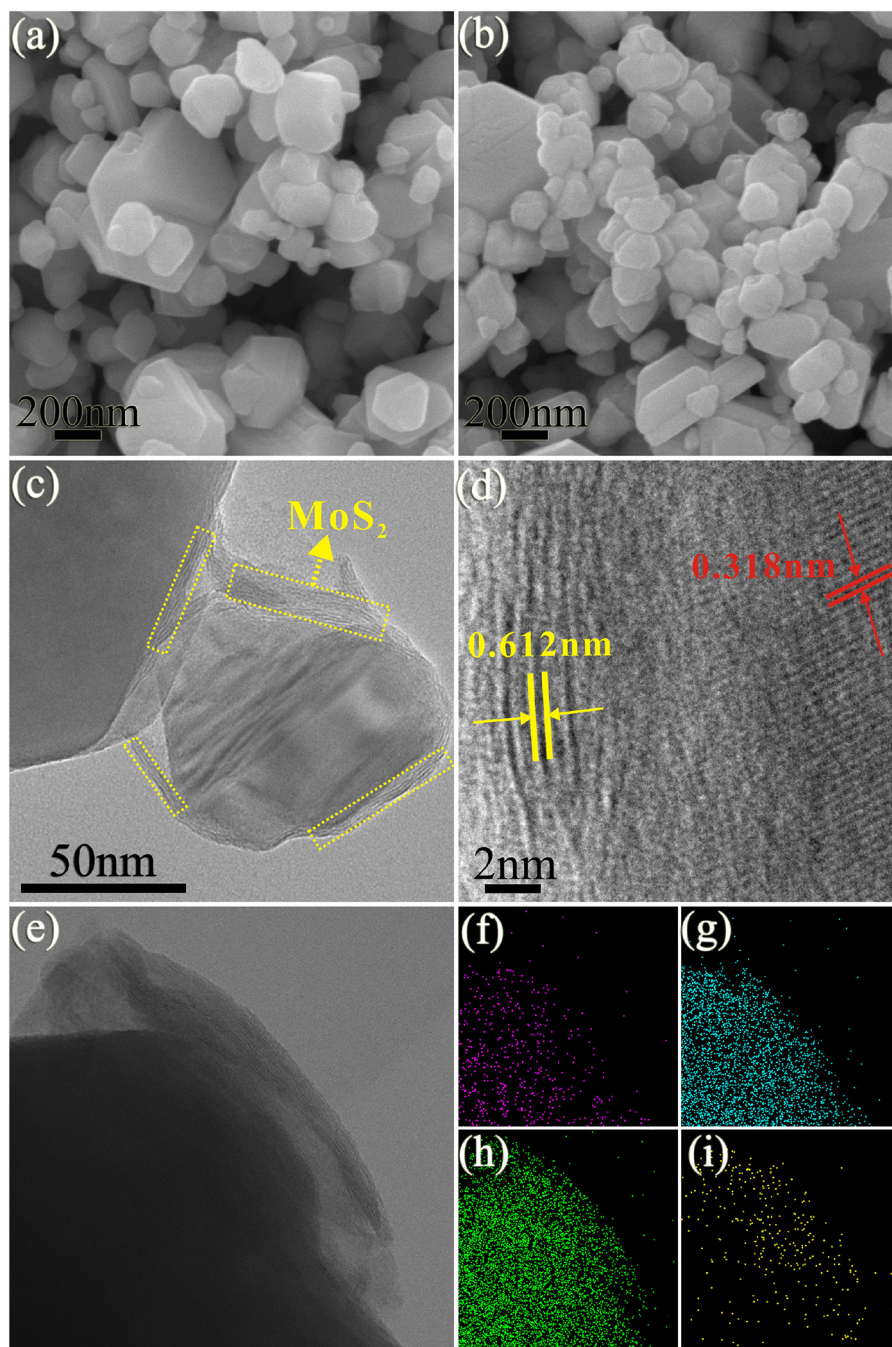
Fig. 2. FE-SEM image of (a) $Mn_{0.25}Cd_{0.75}S$ and (b) $Mn_{0.25}Cd_{0.75}S/MoS_2$-0.7 wt%, TEM (c) and HRTEM (d) image of $Mn_{0.25}Cd_{0.75}S/MoS_2$-0.7 wt%; STEM image (e) of $Mn_{0.25}Cd_{0.75}S/MoS_2$-0.7 wt% and the corresponding element mapping for (f) Mn, (g) Cd, (h) S and (i) Mo.

FE-SEM. As shown in Fig. 2a, $Mn_{0.25}Cd_{0.75}S$ solid solution exhibited polyhedral, well-crystallized morphology and a non-uniform size distribution, varying from 100 nm to 1 μm. However, after loading MoS_2, no obvious difference could be identified between the shapes and surface nanostructures of $Mn_{0.25}Cd_{0.75}S$ (Fig. 2b), suggesting that the MoS_2 loading process did not damage the solid solution structure. The heterostructure between $Mn_{0.25}Cd_{0.75}S$ and MoS_2 was further elucidated using TEM and HRTEM. It was clear that the layered MoS_2 was coated onto the $Mn_{0.25}Cd_{0.75}S$ surface, forming intimate interfaces, as marked by yellow block diagrams in Fig. 2c. From the magnified HRTEM image of the $Mn_{0.25}Cd_{0.75}S/MoS_2$-0.7 wt% composite in Fig. 2d, the lattice fringes of $Mn_{0.25}Cd_{0.75}S$

with a d-spacing of 0.318 nm could be assigned to the (002) lattice plane of $Mn_{0.25}Cd_{0.75}S$. The (002) plane of MoS_2 with a lattice spacing of 0.612 nm was also observed in the composite [42]. Furthermore, the EDS element mapping (Fig. 2e–i) analysis of $Mn_{0.25}Cd_{0.75}S/MoS_2$-0.7 wt% displayed the homogeneous distribution of elemental Cd, Mn and S, as well as the relatively weak signal of Mo matching with the layered structure on the surface of $Mn_{0.25}Cd_{0.75}S$, suggesting the MoS_2 slabs are intimately deposited on the surface of $Mn_{0.25}Cd_{0.75}S$. The excellent interface between $Mn_{0.25}Cd_{0.75}S$ and MoS_2 is expected to not only improve the separation of photogenerated charge carriers but also provide abundant catalytic sites for H_2 evolution.
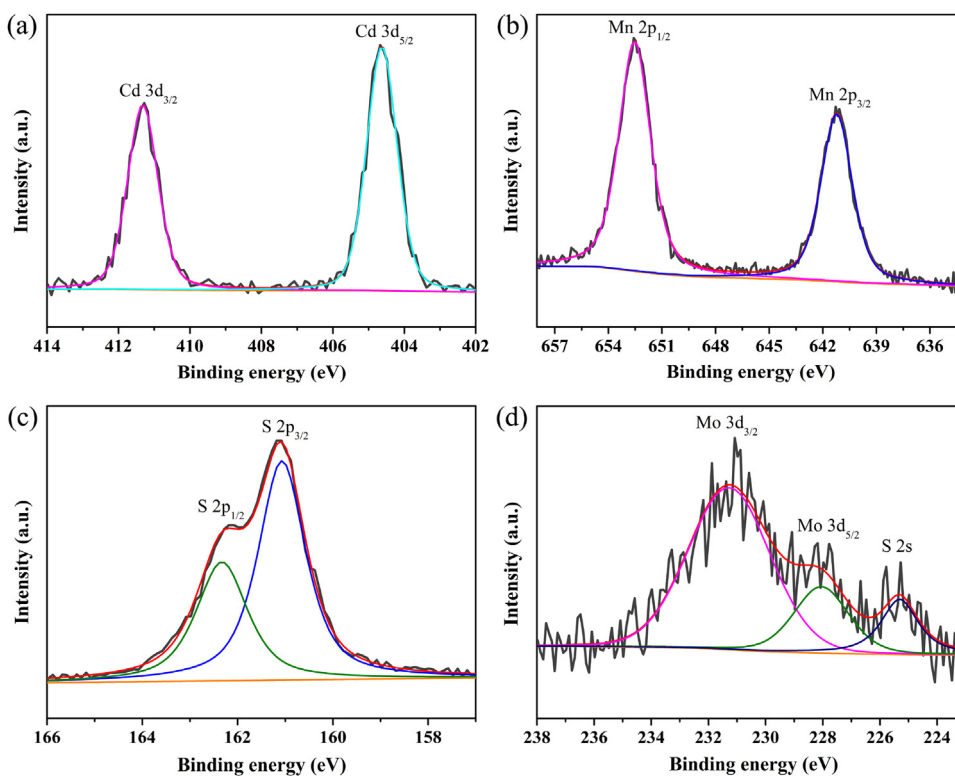
Fig. 3. The high resolution XPS spectra of $Mn_{0.25}Cd_{0.75}S/MoS_2$-0.7 wt% composite for (a) Cd, (b) Mn, (c) S and (d) Mo.

3.3. XPS analysis

The surface elemental composition and oxidation states of the composite material were analyzed using XPS. XPS survey spectra revealed the presence of Cd, Mn, Mo and S (Fig. S3). The oxidation states of the elements were confirmed via the high-resolution XPS spectra of Cd 3d, Mn 2p, Mo 3d and S 2p. Fig. 3a showed the Cd 3d XPS spectrum and the binding energies at 404.7 and 411.3 eV corresponded to Cd $3d_{5/2}$ and Cd $3d_{3/2}$, respectively, confirming the +2 oxidation state of Cd in $Mn_{0.25}Cd_{0.75}S/MoS_2$-0.7 wt%. Mn 2p spectrum displayed two peaks at 652.6 and 641.3 eV, corresponding to $2p_{1/2}$ and $2p_{3/2}$ of Mn^{2+} in composite, respectively (Fig. 3b). In addition, the S 2p peaks were present at binding energies of 161.2 and 162.2 eV, as shown in Fig. 3c. The binding energies of Cd, Mn and S were in good agreement with the reported values [20,31]. Notably, the binding energies of the Mo 3d spectra in Fig. 3d that appeared at 228.1 and 231.3 eV matched well with the binding energy of (Mo $3d_{5/2}$) and 231.1 eV (Mo $3d_{3/2}$) in previous reports [43,44], which indicates that Mo^{4+} is the dominant oxidation state, confirming the presence of MoS_2. XPS result further proved that MoS_2 is deposited on the surface of $Mn_{0.25}Cd_{0.75}S$ solid solution, suggesting the formation of heterostructured composite.

3.4. UV–vis DRS analysis

Fig. 4 showed the UV−vis DRS of $Mn_{0.25}Cd_{0.75}S$, MoS_2 and $Mn_{0.25}Cd_{0.75}S/MoS_2$ composites. Pure $Mn_{0.25}Cd_{0.75}S$ displayed an absorption edge around 550 nm, corresponding to the band gap of 2.26 eV. The inset in Fig. 4 showed that the as-synthesized MoS_2 has a humped absorption peak in the visible light and near-infrared region due to its narrow band gap [45–49]. Compared with pure $Mn_{0.25}Cd_{0.75}S$, $Mn_{0.25}Cd_{0.75}S/MoS_2$ composites could effectively shift the absorption range to 553–607 nm with the increase of MoS_2 content, probably attributing to the intimate interfacial contact between $Mn_{0.25}Cd_{0.75}S$ and MoS_2. Therefore, the light harvesting
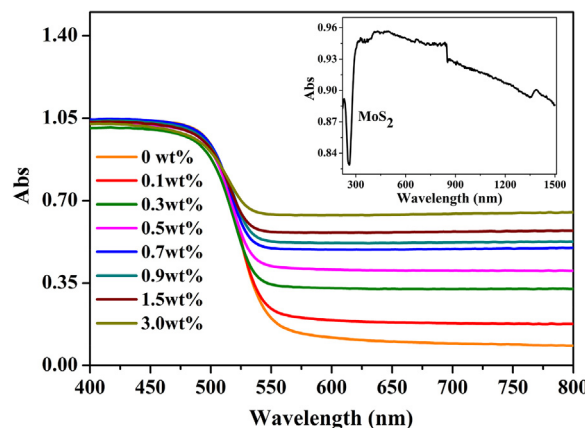

Fig. 4. UV-vis DRS spectra of MoS_2 (inset), $Mn_{0.25}Cd_{0.75}S$ and $Mn_{0.25}Cd_{0.75}S/MoS_2$ composites.

efficiency of the $Mn_{0.25}Cd_{0.75}S/MoS_2$ composites was higher than that of $Mn_{0.25}Cd_{0.75}S$ in the visible light region. It is believed that the enhanced light absorption of $Mn_{0.25}Cd_{0.75}S/MoS_2$ composites is favorable to generate more available photogenerated electrons for participating in the photocatalytic reaction towards H_2 evolution.

3.5. BET surface areas and pore size distributions

Fig. 5 depicted the nitrogen adsorption–desorption isotherms and the corresponding pore size distribution curves of the $Mn_{0.25}Cd_{0.75}S$ and $Mn_{0.25}Cd_{0.75}S/MoS_2$-0.7 wt% samples. Their isotherms could be categorized as type IV and H3 hysteresis loops in the P/P_0 range of 0.9–1.0 [50], indicating the formation of mesopores and macropores due to the random aggregation of samples [5,23]. Pore size distribution curves (inset in Fig. 5) indicated that the two samples exhibit wide pore size distribution from 2 to
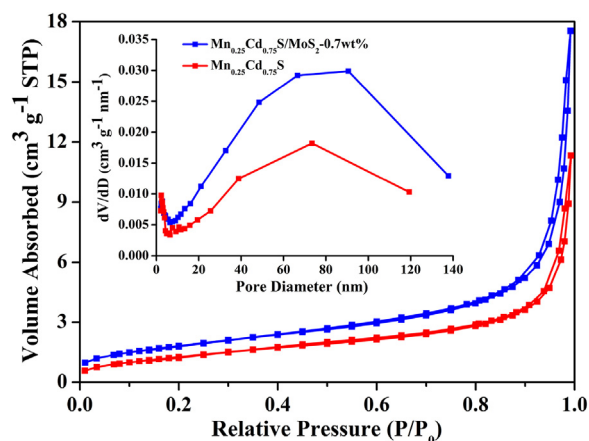
Fig. 5. Nitrogen adsorption–desorption isotherms and corresponding pore size distributions (inset) of the $Mn_{0.25}Cd_{0.75}S$ and $Mn_{0.25}Cd_{0.75}S/MoS_2$-0.7 wt% composite.

Fig. 7. H_2 evolution rate for 4 h over the $Mn_{0.25}Cd_{0.75}S$ solid solution with different mass ratio of MoS_2 under visible light irradiation.
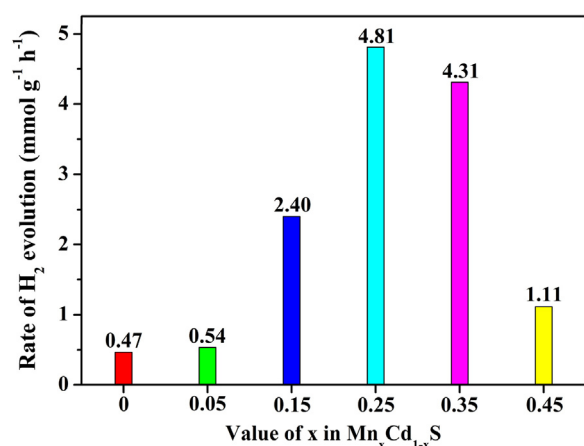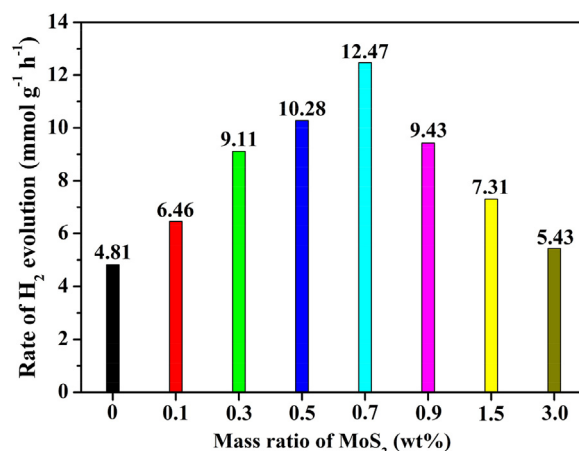

Fig. 6. H_2 evolution rate for 4 h over $Mn_xCd_{1-x}S$ solid solution with different x value $(0.05 \leq x \leq 0.45)$ together with CdS ($x = 0$) under visible light irradiation.

140 nm, further confirming the existence of mesopores and macropores. The obtained BET specific surface area of $Mn_{0.25}Cd_{0.75}S$ was $4.93\,m^2\,g^{-1}$, whereas that of the $Mn_{0.25}Cd_{0.75}S/MoS_2$-0.7 wt% composite slightly increased to $6.74\,m^2\,g^{-1}$. The increased surface area can be attributed to the loading of MoS_2 on the surface of $Mn_{0.25}Cd_{0.75}S$, which may be beneficial for the increase of active sites and enhancement of photocatalytic activity.

3.6. Photocatalytic activity and stability

Photocatalytic H_2 evolution activity of the as-prepared samples was investigated in $0.5\,mol\,L^{-1}$ $Na_2S/0.5\,mol\,L^{-1}$ Na_2SO_3 aqueous solution under visible light irradiation ($\lambda \geq 400\,nm$). Control experiments confirmed that no appreciable H_2 evolution was detected in the absence of either irradiation or photocatalyst, suggesting that H_2 was mainly produced via photocatalytic reactions. The photocatalytic H_2 evolution performance over pure $Mn_xCd_{1-x}S$ solid solution together with CdS under visible-light irradiation for 4 h was shown in Fig. 6. The rate of H_2 evolved from pure CdS was low ($0.47\,mmol\,g^{-1}\,h^{-1}$) mainly due to its poor separation ability of photogenerated charge carriers [12]. After the incorporation of Mn^{2+} ions, the activities for H_2 evolution increased dramatically with increasing values of x from 0.05 to 0.25. The H_2 evolution rate over the $Mn_{0.05}Cd_{0.95}S$ sample was as high as $0.54\,mmol\,g^{-1}\,h^{-1}$ and further increased to $2.40\,mmol\,g^{-1}\,h^{-1}$ over $Mn_{0.15}Cd_{0.85}S$ sample. In particular, $Mn_{0.25}Cd_{0.75}S$ solid solution showed the highest H_2 evolution rate of approximately $4.81\,mmol\,g^{-1}\,h^{-1}$, which is

about 10 times higher than that over CdS alone. However, with further increasing the value of x, the photocatalytic activity of the solid solution decreased, but it is still higher than that of pure CdS. According to the above results, it was clearly seen that the photocatalytic activity of CdS has been dramatically improved by the formation of $Mn_xCd_{1-x}S$ solid solutions. Moreover, the photocatalytic abilities of $Mn_xCd_{1-x}S$ solid solutions were closely dependent on their corresponding compositions. In this research, the optimized solid solution was proved to be $Mn_{0.25}Cd_{0.75}S$, suggesting its suitable band gap and position are best for the visible-light-driven photocatalytic H_2 evolution from water splitting.

Fig. 7 showed the comparison of the average photocatalytic H_2 evolution rate over $Mn_{0.25}Cd_{0.75}S/MoS_2$ composites with different weight percentage of MoS_2 under visible light irradiation for 4 h. No H_2 was detected when MoS_2 alone was used as the catalyst, suggesting that MoS_2 is not active for photocatalytic H_2 evolution. As observed in Fig. 7, $Mn_{0.25}Cd_{0.75}S$ alone exhibited a H_2 evolution rate of $4.81\,mmol\,g^{-1}\,h^{-1}$. The relatively low activity of pure $Mn_{0.25}Cd_{0.75}S$ could be attributed to the fast recombination of photogenerated electron–hole pairs. After loading only 0.1 wt% of MoS_2 on $Mn_{0.25}Cd_{0.75}S$, the rate was increased to $6.46\,mmol\,g^{-1}\,h^{-1}$. With the increase of the loading content of MoS_2, the H_2 evolution rate of $Mn_{0.25}Cd_{0.75}S/MoS_2$ composite was further increased initially. In particular, the composite with the MoS_2 loading amount of 0.7 wt% showed the highest H_2 evolution rate of $12.47\,mmol\,g^{-1}\,h^{-1}$, which is about 2.6 time higher that of $Mn_{0.25}Cd_{0.75}S$ alone. The corresponding apparent quantum efficiency (AQE) at 420 nm reached 2.37% for the $Mn_{0.25}Cd_{0.75}S/MoS_2$-0.7 wt% photocatalyst. Further loading of MoS_2 onto $Mn_{0.25}Cd_{0.75}S$ led to a decrease in the photocatalytic activity due to the following two aspects: (i) the color of the composites turned much deeper ranging from orange to dark-green with increasing the loading content of black MoS_2, demonstrating that the introduction of a large percentage of black MoS_2 can significantly increase the opacity and shield the incident light from irradiating the photocatalyst; (ii) the active sites were likely to be blocked by excess MoS_2 co-catalyst, which hinders the effective contact between the active sites and the reactants. Therefore, loading appropriate amounts of MoS_2 co-catalyst can optimize the photocatalytic activity of the $Mn_{0.25}Cd_{0.75}S$ solid solution.

For comparison, the most commonly used noble metal Pt was also tested as the H_2 evolution co-catalysts. 1.0 wt% of Pt co-catalyst was loaded onto the surface of $Mn_{0.25}Cd_{0.75}S$ by the typical photodeposition method using H_2PtCl_6 as the precursor. The time-online photocatalytic H_2 evolution test in Fig. 8 indicated that loading of Pt significantly enhances the H_2 evolution activity of
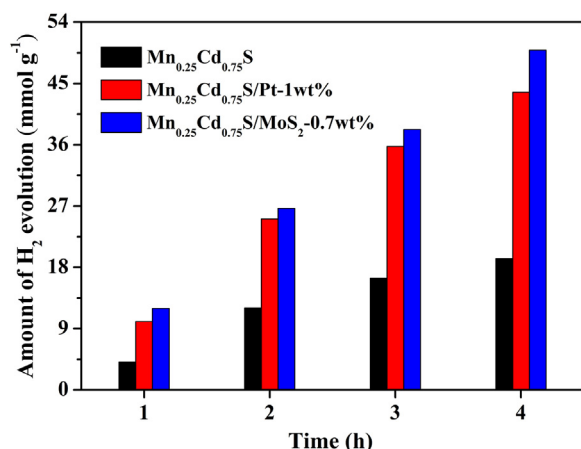
Fig. 8. Comparison of H_2 evolution activity of $Mn_{0.25}Cd_{0.75}S/MoS_2$-0.7 wt% with $Mn_{0.25}Cd_{0.75}S/Pt$-1 wt% and $Mn_{0.25}Cd_{0.75}S$ under visible light irradiation.
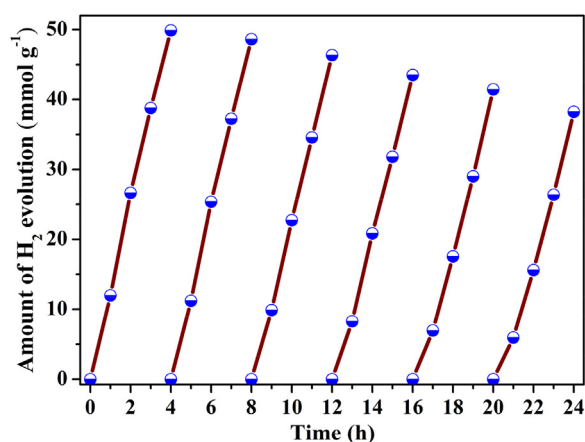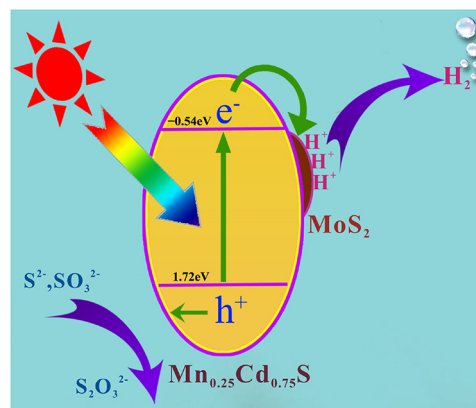

Scheme 1. Schematic illustration of proposed mechanism for the enhanced photocatalytic H_2 evolution.

Fig. 9. Cycling test of photocatalytic H_2 evolution over $Mn_{0.25}Cd_{0.75}S/MoS_2$-0.7 wt% under visible light irradiation.

$Mn_{0.25}Cd_{0.75}S$. The H_2 evolution amount over $Mn_{0.25}Cd_{0.75}S/Pt$-1.0 wt% reached 43.68 mmol g^{-1} after visible light irradiation of 4 h, which is much higher than that of pure $Mn_{0.25}Cd_{0.75}S$ (19.25 mmol g^{-1}). However, the value is still slightly lower than that of $Mn_{0.25}Cd_{0.75}S/MoS_2$-0.7 wt%, indicating that MoS_2 is an excellent co-catalyst for promoting highly efficient photocatalytic H_2 evolution in the present system. The results indicated that co-catalyst modification of MoS_2 is a simpler yet more efficient approach for enhancing the activity of $Mn_{0.25}Cd_{0.75}S$, further confirming the important functions of the heterojunction between MoS_2 and $Mn_{0.25}Cd_{0.75}S$ in enhancing the H_2 evolution activity.

Apart from activity, the stability of a given photocatalyst is very crucial for its practical application. To confirm the stability of $Mn_{0.25}Cd_{0.75}S/MoS_2$ samples, we performed six consecutive H_2 evolution runs over the best sample, $Mn_{0.25}Cd_{0.75}S/MoS_2$-0.7 wt%, under the same conditions. Each cycle was performed for 4 h under visible light illumination. Fig. 9 displayed the recycling photocatalytic stability of the $Mn_{0.25}Cd_{0.75}S/MoS_2$-0.7 wt% composite under visible light irradiation ($\lambda \geq 400$ nm). After six recycles, a total of 38.23 mmol g^{-1} H_2 was produced, which is almost 23% of H_2 production activity loss, indicating the relative good photostability of $Mn_{0.25}Cd_{0.75}S/MoS_2$ composite for photocatalytic H_2 evolution.

3.7. The charge-separation and proposed mechanism

To understand the efficiency of charge transfer and separation in $Mn_{0.25}Cd_{0.75}S/MoS_2$ composite, photoluminescence (PL)

spectra and time-resolved photoluminescence (TRPL) spectra of $Mn_{0.25}Cd_{0.75}S$ and $Mn_{0.25}Cd_{0.75}S/MoS_2$-0.7 wt% composite were investigated. Fig. 10a showed PL spectra of $Mn_{0.25}Cd_{0.75}S$ and $Mn_{0.25}Cd_{0.75}S/MoS_2$-0.7 wt% composite at an excitation wavelength of 331 nm, and an emission peak at 539 nm could be observed. It was obvious that the emission was remarkably quenched upon loading MoS_2, attributing to the fast transfer of electrons from $Mn_{0.25}Cd_{0.75}S$ to MoS_2, which could suppress the electron–hole recombination and enhance the photocatalytic activity. Charge carrier lifetime plays an important role in photocatalytic reactions, the longer charge carrier lifetime lasts, more photo-generated electrons and holes participate in photocatalytic reactions. As shown in Fig. 10b, the TRPL spectra further indicated that the charge carriers lifetime of $Mn_{0.25}Cd_{0.75}S/MoS_2$-0.7 wt% (1.885 ns) is higher than that of pure $Mn_{0.25}Cd_{0.75}S$ (1.5058 ns), also indicating that MoS_2 is an effective co-catalyst for charge transfer.

The interface charge separation efficiency can be further investigated by the photoelectrochemical technique. The periodic on/off photocurrent response of the $Mn_{0.25}Cd_{0.75}S$ and $Mn_{0.25}Cd_{0.75}S/MoS_2$-0.7 wt% composite under the irradiation of visible light was also investigated to confirm the promoted separation efficiency of photo-generated carriers. As indicated in Fig. 11a, the composite exhibited a much higher photocurrent density compared to $Mn_{0.25}Cd_{0.75}S$ under the same condition, which was contributed to the efficient photogenerated electron transfer from $Mn_{0.25}Cd_{0.75}S$ to MoS_2. Since electrochemical impedance spectroscopy (EIS) is one of the most powerful techniques to deeply investigate the migration and interface transfer/recombination rates of charge carriers, the EIS Nyquist plots of pure $Mn_{0.25}Cd_{0.75}S$ and $Mn_{0.25}Cd_{0.75}S/MoS_2$-0.7 wt% were also performed to investigate the complicated interfacial effect between MoS_2 and $Mn_{0.25}Cd_{0.75}S$. As displayed in Fig. 11b, it was obviously that $Mn_{0.25}Cd_{0.75}S/MoS_2$ composite exhibited a small arc size in the middle-frequency region as compared to pure $Mn_{0.25}Cd_{0.75}S$, suggesting the faster electron transfer through an intimated interface between $Mn_{0.25}Cd_{0.75}S$ and MoS_2, which was in good agreement with the photocatalytic performance.

Based on all the above results, a proposed mechanism for the enhanced photocatalytic H_2 evolution activities of $Mn_{0.25}Cd_{0.75}S/MoS_2$ photocatalysts was illustrated in Scheme 1. First of all, the valence band (VB) and conduction band (CB) potential of $Mn_{0.25}Cd_{0.75}S$ were determined because the band structure of a photocatalyst can affect its photocatalytic ability. The VB potential of $Mn_{0.25}Cd_{0.75}S$ was determined to be 1.72 eV according to its VB XPS spectra (Fig. S4). Then the CB potential of $Mn_{0.25}Cd_{0.75}S$ was calculated to be -0.54 eV by the equation of $E_{CB} = E_{VB} - E_g$. It is known that the CB minimum position of few-layer MoS_2 locates at
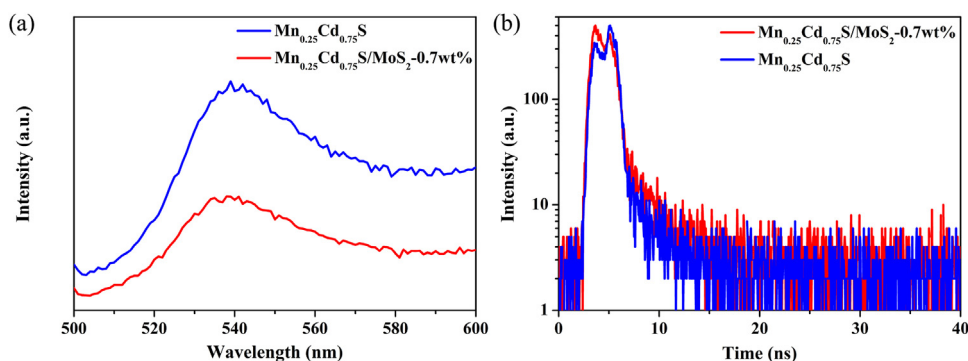
Fig. 10. (a) PL spectra of $Mn_{0.25}Cd_{0.75}S$ and $Mn_{0.25}Cd_{0.75}S/MoS_2$-0.7 wt% composite ($\lambda_{exc}$ = 331 nm), (b) TRPL spectra for $Mn_{0.25}Cd_{0.75}S$ and $Mn_{0.25}Cd_{0.75}S/MoS_2$-0.7 wt% composite detected at 539 nm, the excitation source is a 377.8 nm laser.
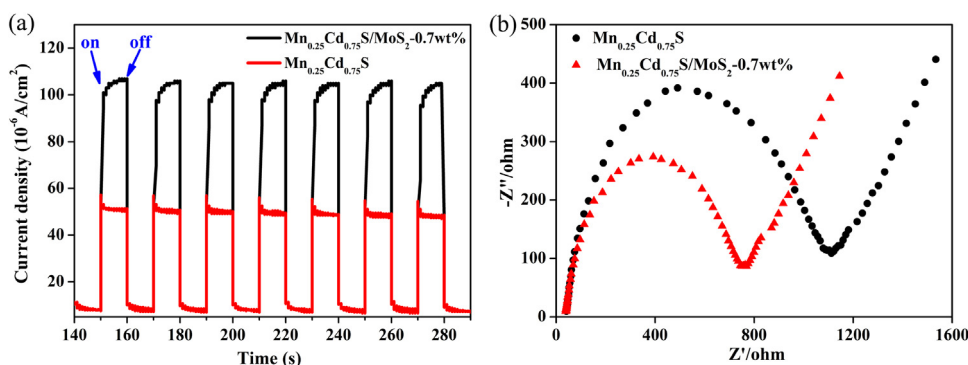

Fig. 11. (a) I–t curves and (b) EIS Nyquist plots of $Mn_{0.25}Cd_{0.75}S$ and $Mn_{0.25}Cd_{0.75}S/MoS_2$-0.7 wt%.

−0.13 eV [33,35,51] vs. 0 V of H^+/H_2 potential. Therefore, compared to MoS_2, the more negative CB level of $Mn_{0.25}Cd_{0.75}S$ facilitates to provide ample thermodynamic driving force for the photogenerated electrons transfer from the CB of $Mn_{0.25}Cd_{0.75}S$ to that of layered MoS_2. In addition, the intimate interfacial contact between $Mn_{0.25}Cd_{0.75}S$ and MoS_2 also helps to promote the electrons transfer from $Mn_{0.25}Cd_{0.75}S$ to MoS_2. More importantly, it was revealed that the unsaturated active S atoms on exposed edges of MoS_2 could act as the active sites and promote the dissociation of water and the evolution of H_2 [21,25,26,32,52–54]. To sum up, under visible light irradiation, $Mn_{0.25}Cd_{0.75}S$ was excited and generated electron–hole pairs. The photogenerated electrons in the CB of $Mn_{0.25}Cd_{0.75}S$ could be easily transferred to MoS_2 due to the intimate interfacial contact between $Mn_{0.25}Cd_{0.75}S$ and MoS_2, effectively decreasing the recombination of photogenerated electrons and holes. Then the trapped electrons on the surface of MoS_2 directly reacted with the adsorbed H^+ ions at the edges of MoS_2 to efficiently produce H_2. Meantime, the holes in the VB of $Mn_{0.25}Cd_{0.75}S$ would be transferred to surface and trapped by the sacrificial reagents (Na_2S and Na_2SO_3), further boosting charge separation. As a result, the co-catalyst MoS_2 loading on $Mn_{0.25}Cd_{0.75}S$ accelerated the separation of the photogenerated charge carriers and provided abundant reactive sites, contributing to outstanding photocatalytic activity for H_2 evolution.

4. Conclusions

In summary, a series of novel $Mn_{0.25}Cd_{0.75}S/MoS_2$ composites were rationally designed and prepared by a facile one-step hydrothermal method. The characterizations demonstrated that the layered MoS_2 was tightly loaded on the surface of $Mn_{0.25}Cd_{0.75}S$. The intimate interface between $Mn_{0.25}Cd_{0.75}S$ and MoS_2 not only facilitated the charge separation and transfer but also

provided more active sites for H_2 evolution reaction. As a result, through the optimizing of the MoS_2 loading content, the $Mn_{0.25}Cd_{0.75}S/MoS_2$ composite showed the highest photocatalytic activity when the content of the MoS_2 was 0.7 wt%, giving a H_2 evolution rate of 12.47 mmol g^{-1} h^{-1}, which is much higher than that of $Mn_{0.25}Cd_{0.75}S$ and also slightly higher than that of $Mn_{0.25}Cd_{0.75}S/Pt$ (1.0 wt%). It is believed that this kind of noble-metal-free $Mn_{0.25}Cd_{0.75}S/MoS_2$ composite has great potential for photocatalytic H_2 evolution under visible light irradiation.

Appendix A. Supplementary data

Supplementary data associated with this article can be found, in the online version, at http://dx.doi.org/10.1016/j.apcatb.2017.03.035.

References

[1] A. Fujishima, K. Honda, Nature 238 (1972) 37–38.
[2] J. Li, J.H. Yang, F.Y. Wen, C. Li, Chem. Commun. 47 (2011) 7080–7082.
[3] M. Zhong, J.Y. Shi, F.Q. Xiong, W.H. Zhang, C. Li, Sol. Energy 86 (2012) 756–763.
[4] X. Jia, M. Tahir, L. Pan, Z.F. Huang, X.W. Zhang, L. Wang, J.J. Zou, Appl. Catal. B 198 (2016) 154–161.
[5] J.L. Yuan, J.Q. Wen, Q.Z. Gao, S.C. Chen, J.M. Li, X. Li, Y.P. Fang, Dalton Trans. 44 (2015) 1680–1689.
[6] A. Kudo, Y. Miseki, Chem. Soc. Rev. 38 (2009) 253–278.
[7] Z. Yan, X. Yu, A. Han, P. Xu, P. Du, J. Phys. Chem. C 118 (2014) 22896–22903.

[8] Z. Yan, X. Yu, Y. Zhang, H. Jia, Z. Sun, P. Du, Appl. Catal. B 160 (2014) 173–178.
[9] Y.B. Wang, J.C. Wu, J.W. Zheng, R. Xu, Catal. Sci. Technol. 1 (2011) 940–947.
[10] D.H. Wang, L. Wang, A.W. Xu, Nanoscale 4 (2012) 2046–2053.
[11] K. Ikeue, S. Shiiba, M. Machida, Chem. Mater. 22 (2010) 743–745.
[12] M.Y. Liu, L.Q. Zhang, X.X. He, B. Zhang, H.F. Song, S.N. Li, W.S. You, J. Mater. Chem. A 2 (2014) 4619–4626.
[13] J.S. Lai, Y.M. Qin, L. Yu, C.Y. Zhang, Mater. Sci. Semicond. Process. 52 (2016) 82–90.
[14] L. Ren, F. Yang, Y.R. Deng, N.N. Yan, S. Huang, D. Lei, Q. Sun, Y. Yu, Int. J. Hydrogen Energy 35 (2010) 3297–3305.
[15] Y.H. Lin, F. Zhang, D.C. Pan, J. Mater. Chem. 22 (2012) 22619–22623.
[16] K. Zhang, L.J. Guo, Catal. Sci. Technol. 3 (2013) 1672–1690.
[17] G.J. Liu, Z.H. Zhou, L.J. Guo, Chem. Phys. Lett. 509 (2011) 43–47.
[18] K. Ikeue, S. Shiiba, M. Machida, ChemSusChem 4 (2011) 269–273.
[19] K. Ikeue, Y. Shinmura, M. Machida, Appl. Catal. B 123–124 (2012) 84–88.
[20] H. Liu, Z.Z. Xu, Z. Zhang, D. Ao, Appl. Catal. A 518 (2016) 150–157.
[21] S. Ma, J. Xie, J.Q. Wen, K.L. He, X. Li, W. Liu, X.C. Zhang, Appl. Surf. Sci. 391 (2017) 580–591.
[22] Y.J. Yuan, J.R. Tu, Z.J. Ye, D.Q. Chen, B. Hu, Y.W. Huang, T.T. Chen, D.P. Cao, Z.T. Yu, Z.G. Zou, Appl. Catal. B 188 (2016) 13–22.
[23] T.M. Di, B.C. Zhu, J. Zhang, B. Cheng, J.G. Yu, Appl. Surf. Sci. 389 (2016) 775–782.
[24] W.J. Jiang, Y.F. Liu, R.L. Zong, Z.P. Li, W.Q. Yao, Y.F. Zhu, J. Mater. Chem. A 3 (2015) 18406–18412.
[25] Y.Y. Zhu, Q. Ling, Y.F. Liu, H. Wang, Y.F. Zhu, Phys. Chem. Chem. Phys. 17 (2015) 933–940.
[26] X.L. Yu, R.F. Du, B.Y. Li, Y.H. Zhang, H.J. Liu, J.H. Qu, X.Q. An, Appl. Catal. B 182 (2016) 504–512.
[27] S. Cao, C.J. Wang, X.J. Lv, Y. Chen, W.F. Fu, Appl. Catal. B 162 (2015) 381–391.
[28] M.G. Walter, E.L. Warren, J.R. McKone, S.W. Boettcher, Q. Mi, E.A. Santori, N.S. Lewis, Chem. Rev. 110 (2010) 6446–6473.
[29] N.Z. Bao, L.M. Shen, T. Takata, K. Domen, Chem. Mater. 20 (2008) 110–117.
[30] H. Yan, J. Yang, G. Ma, G. Wu, X. Zong, Z. Lei, J. Shi, C. Li, J. Catal. 266 (2009) 165–168.
[31] X.L. Liu, X.Z. Liang, P. Wang, B.B. Huang, X.Y. Qin, X.Y. Zhang, Y. Dai, Appl. Catal. B 203 (2017) 282–288.
[32] X. Zong, H. Yan, G. Wu, G. Ma, F. Wen, L. Wang, C. Li, J. Am. Chem. Soc. 130 (2008) 7176–7177.
[33] X.L. Yin, L.L. Li, W.J. Jiang, Y. Zhang, X. Zhang, L.J. Wan, J.S. Hu, ACS Appl. Mater. Interfaces 8 (2016) 15258–15266.
[34] D.P. Kumar, S. Hong, D.A. Reddy, T.K. Kim, J. Mater. Chem. A 4 (2016) 18551–18558.
[35] X.L. Yin, G.Y. He, B. Sun, W.J. Jiang, D.J. Xue, A.D. Xia, L.J. Wan, J.S. Hu, Nano Energy 28 (2016) 319–329.
[36] Z. Lv, N. Mahmood, M. Tahir, L. Pan, X.W. Zhang, J.J. Zou, Nanoscale 8 (2016) 18250–18269.
[37] L. Vegard, H. Schjelderup, Phys. Z 18 (1917) 93–96.
[38] J.K. Furdyna, J. Appl. Phys. 64 (1988) 3663–3664.
[39] I. Tsuji, H. Kato, H. Kobayashi, A. Kudo, J. Am. Chem. Soc. 126 (2004) 13406–13413.
[40] C.H. An, K.B. Tang, X.M. Liu, F.Q. Li, G.E. Zhou, Y.T. Qian, J. Cryst. Growth 252 (2003) 575–580.
[41] D.B. Fan, X.D. Yang, H. Wang, Y.C. Zhang, H. Yan, Physica B 337 (2003) 165–169.
[42] M.Q. Yang, C. Han, Y.J. Xu, J. Phys. Chem. C 119 (2015) 27234–27246.
[43] W.K. Jo, T. Adinaveen, J.J. Vijaya, N.C.S. Selvam, RSC Adv. 6 (2016) 10487–10497.
[44] B. Chen, N.Q. Zhao, L.C. Guo, F. He, C.S. Shi, C.N. He, J.J. Li, E.Z. Liu, Nanoscale 7 (2015) 12895–12905.
[45] W. Zhou, Z. Yin, Y. Du, X. Huang, Z. Zeng, Z. Fan, H. Liu, J. Wang, H. Zhang, Small 9 (2013) 140–147.
[46] W. Ho, J.C. Yu, J. Lin, J.G. Yu, P.S. Li, Langmuir 20 (2004) 5865–5869.
[47] N. Singh, G. Jabbour, U. Schwingenschlögl, Eur. Phys. J. B 85 (2012) 392.
[48] J.K. Ellis, M.J. Lucero, G.E. Scuseria, Appl. Phys. Lett. 99 (2011) 261908.
[49] K. Chang, M. Li, T. Wang, S.X. Ouyang, P. Li, L.Q. Liu, J.H. Ye, Adv. Energy Mater. (2015) 1402279.
[50] K.S.W. Sing, D.H. Everett, R.A.W. Haul, L. Moscou, R.A. Pierotti, J. Rouquérol, T. Siemieniewska, Pure Appl. Chem. 57 (1985) 603–619.
[51] Y.G. Li, H.L. Wang, L.M. Xie, Y.Y. Liang, G.S. Hong, H.J. Dai, J. Am. Chem. Soc. 133 (2011) 7296–7299.
[52] T.F. Jaramillo, K.P. Jørgensen, J. Bonde, J.H. Nielsen, S. Horch, I. Chorkendorff, Science 317 (2007) 100–102.
[53] K. Chang, Z.W. Mei, T. Wang, Q. Kang, S.X. Ouyang, J.H. Ye, ACS Nano 8 (2014) 7078–7087.
[54] H.G. Yu, P. Xiao, P. Wang, J.G. Yu, Appl. Catal. B 193 (2016) 217–225.